IEEE Open Journal of
Power Electronics

Received 27 October 2025; revised 3 December 2025; accepted 12 December 2025. Date of publication 30 December 2025; date of current version 8 January 2026. The review of this article was arranged by Associate Editor Lin Qiu.

Digital Object Identifier 10.1109/OJPEL.2025.3644589

Lumped Thermal Model for Magnetic Components in an Interleaved DC–DC Converter

MOHAMMAD SHAHJALAL [1], **UVAIS MUSTAFA** [2] **(Member, IEEE),**
STOYAN STOYANOV [3] **(Senior Member, IEEE), AND MD. RISHAD AHMED** [4] **(Member, IEEE)**

School of Computing and Mathematical Sciences, University of Greenwich, London SE10 9LS, U.K.
Power Electronics, Machines and Control Group, University of Nottingham, Nottingham NG7 2RD, U.K.
School of Computing and Mathematical Sciences, University of Greenwich, London SE10 9LS, U.K.
Power Electronics, Machines and Control Group, University of Nottingham, Nottingham NG7 2RD, U.K.

CORRESPONDING AUTHOR: UVAIS MUSTAFA (e-mail: uvais.mustafa@nottingham.ac.uk)

This work was supported by the Engineering and Physical Sciences Research Council under Grant EP/S024069/1. The work was conducted within the Centre for Doctoral Training in Sustainable Electric Propulsion.

ABSTRACT Magnetic component design is one of the key challenges for high-frequency DC-DC converters. Simple loss-based thermal analysis can be an alternative to achieving an effective electrothermal design for magnetics at the initial design stage, before the real prototype design, which can save cost and time. In this paper, a lumped thermal equivalent circuit (LTEC) model is developed to guide the thermal design of magnetic components. LTEC models are compared with finite element analysis (FEA) and experimental results. To capitalise on the amorphous core in designing high-current/high-frequency magnetic components, a physics-based analytical thermal model can be used to identify temperatures at specific nodes or points of interest. This lumped parameter-based method can be used for quick analysis and design optimisation, whereas FEA is better for identifying accurate temperature distribution and hot-spot temperatures and to guide the designers to achieve effective thermal design by adopting appropriate strategies such as potting or liquid cooling. This paper investigates two magnetic components in a high-frequency, interleaved DC-DC converter: one is the high current filter inductor, and the other is the interphase transformer (IPT). Both LTEC and FEA models are validated using experimental measurements from a 1.5 kW interleaved DC-DC converter prototype. The proposed LTEC results are comparable to both experimental and FEA results, and for the inductor, the average error is limited to 7.4% while for the IPT transformer average error is up to 5.7% .

INDEX TERMS Electrothermal model, MOSFET(CoolMOS), circuit simulator, finite element analysis, DC–DC converter.

I. INTRODUCTION

Power electronics converter design is still multi-physics oriented and tightly linked to its electrical, thermal and electromagnetic behaviour. Continuous efforts are made to achieve high-performance converters by improving power density and efficiency [1], [2]. Efficient and compact converters are required in numerous applications, from electric vehicles to more electrified aircraft. One of the key challenges in designing multi-kW DC-DC converters is the design of high-frequency magnetic components. Magnetic components take up significant space and weight in a converter. For example, in some cases, it can account for 30–50% of the overall converter weight [3], [4]. Therefore, miniaturisation of magnetic components is essential and can help meet converter performance targets. However, it becomes more challenging to tackle thermal management with a reduced surface/volume ratio. Many design options exist for passive components' size reduction. One of the widely established approaches is the use of increased switching frequency in converters, which can help reduce the size of passive components. However, a subsequent increase in switching losses can incur a large heatsink penalty for active components, while in magnetic components, increased core losses can raise their temperature and can cause thermal issues.

Wideband gap semiconductor devices such as silicon carbide (SiC) or gallium nitride (GaN) devices are used in high-frequency, power-dense converters due to their fast-switching speed. However, miniaturisation of magnetic components is still quite challenging. Since the thermal design dictates component reliability in terms of safe operation, it is important to focus on the thermal issues of magnetic components at the initial stage of the converter design. Machine Learning and reduced order approach has been applied for the thermal behaviour prediction in the transformers and inductors [5], [6], [7] and they offer a quick and precise solution and can even predict the temperature changes across the whole geometry of the core and windings with some training on FEA models however, they lose the transparency and the physical interpretability, as they provide a "data-driven model" kind of solution with no way to tell why and how model made those predictions.

Another popular approach for thermal analysis is lumped thermal modelling [8], [9] which can provide fast temperature prediction. Several lumped electrothermal models exist for inductor design in the literature. These are mainly based on lumped nodal temperature prediction. A detailed lumped thermal network for a pre-biased inductor is demonstrated in [10] Using the losses computed from electromagnetic finite element simulations. Further in [11] A generalised 3D cuboidal element is demonstrated to design an inductor. This approach has been further extended to study the potted structured inductor that is mounted onto a forced air-cooled heatsink. The work investigated the use of a ceramic heat spreader to reduce the air-gap temperature. These Lumped Thermal Equivalent Circuit (LTEC) models are directly derived from the physics of heat flow and correspond to real physical parts like thermal resistances and capacitances between different layers and components. The thermal parameters can be easily estimated with geometry and material properties, making the whole LTEC approach easy to validate experimentally, and it can also be used for the ageing-sensitivity analysis.

Sometimes, for detailed analysis, FEA simulations are conducted when total heat distribution, overall thermal mapping across the component and thermal interaction with other components are needed. FEA methods have already demonstrated its potential in transformer/inductor design and loss modelling of magnetic components [12], [13]. FEA-driven thermal analysis has demonstrated the potential of a ceramic heat spreader as part of effective thermal management for gapped nanocrystalline inductors, where localised gap losses act as a prominent heat source [14]. This can be extended to design compact magnetic components for high-frequency converters. However, FEA techniques are quite complex and time-consuming to implement, even though they provide detailed design insights. Lumped Thermal Equivalent Circuit (LTEC) models can provide sufficient information to validate designs at the initial stage of magnetic component development.

Because the lumped thermal modelling approach is relatively quick and easy to implement, it is getting popular for the early design phases. This paper presents a Lumped Thermal Equivalent Circuit (LTEC) modelling method to study and design magnetic components in an interleaved DC-DC converter. A detailed analysis is presented to identify the temperature around the gap of the filter inductor and the hot spot of the IPT. Analytical loss analysis creates the basis for the thermal design of these magnetic components. The estimated loss works as a heat source in the thermal model later in FEA and LTEC models. Simulation results from both LTEC and FEA models are verified with the experimentally achieved thermal data using infrared thermography from a 12V to 48V, 1.5 kW DC-DC converter.

The modelling technique has been adopted from [8]. The work in [8] considered a potted inductor, which was mounted on the air-cooled heatsink. The model described the heat transfer by the potting structure, which was represented by a uniform boundary for thermal modelling. Good thermal contact existed since potting materials filled all the spaces between the windings and the core, including the air gaps between winding turns. The inductor designed in this work is not potted and thus, windings are directly exposed to the ambient boundary condition. This work has also included IPT structure, which is also different from a high current filter inductor since its winding is surrounded by core.

The novelty of the paper can be summarized in the following points: (1) a fast and accurate temperature prediction of magnetic components by multiple nodes considering three-dimensional geometry and its anisotropic characteristics (2) simple prediction and calculation equations for thermal resistance by using magnetic component geometry and datasheet information and (3) identifying the use of equivalent circuit based thermal lumped model for design and optimization of magnetic components, comparing it to FEA methods. (4) Presenting the methodology for the LTEC modelling for different magnetic components (inductors and IPT) with different core geometries and materials to establish the universal nature of the method. In comparison to [5], where the authors used a potted inductor, which has a uniform thermal boundary, the magnetic components in this work are non-potted, and they have different thermal boundary conditions and follow a different heat-flow physics. Additionally, this work validates the application of LTEC modelling for two different geometries and core materials for non-potted magnetic components.

In this paper, Section II describes the modelling framework, loss analysis, FEA set up and design of magnetic components. Section III investigates the thermal performance of magnetic components and compares the proposed modelling results with experimental results. Section IV shows experimental validation. Finally, Section V draws some conclusions about the work.

II. METHODOLOGY

A. MODELLING FRAMEWORK

The modelling method is illustrated in Fig. 1. The First step is to define the geometry of the magnetic component. Once the geometry of the core is identified, the second step is to identify

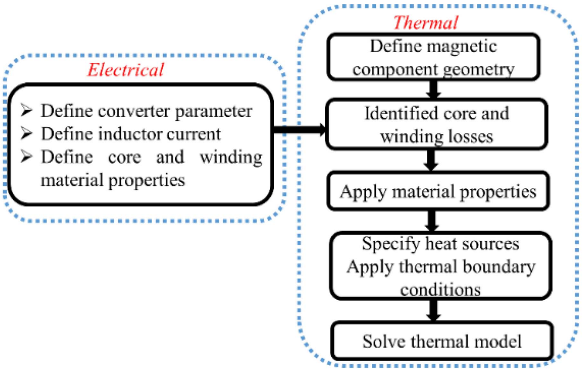

FIGURE 1. **Schematic Description of the proposed modelling method.**

losses using electrical simulation or analytical calculation. Both FEA and LTEC models need material properties for thermal and magnetic analysis; hence, the third step is to define material properties. The fourth step is to define volumetric losses in different regions of the design domain. The identified losses, such as winding losses and core losses, can be used as volumetric heat sources in the thermal models. With the estimated losses in the magnetic component, a commercial FEA software package (COMSOL) can be used to evaluate the temperature distribution. LTEC models are simulated in the Simulink software.

B. MAGNETIC COMPONENT'S DESIGN AND LOSS ESTIMATION

In order to design the magnetics for an interleaved DC-DC converter (Fig. 11), the peak flux density for the core (B), maximum current density for the winding (J) , relative magnetic permittivity (μ_r) and fill factor (k) need to be defined. These parameters are utilised to calculate the number of turns. For the given current flowing through the inductor (I_{in}), the number of turns (N) can be calculated by using (1), which is based on the constraint that the peak flux density in a core should not exceed a predefined maximum value B_{sat}. A_e is the effective core cross-sectional area.

$$N = \frac{L * I_{in}}{B_{sat} .A_e} \tag{1}$$

A C-shaped METGLAS core (AMCC-6.3) with enough winding window is selected to accommodate all the winding turns of the inductor. The dimensions of a C-shaped inductor core are described by these parameters: core limb width (a), window width (b), window length (c), core thickness (d), core width (e), and core height (f). From these parameters, the window space can be calculated for a given winding turn number. The cross-section area for a turn can be calculated using (2).

$$A_{w1} = \frac{I_{in}}{J} \tag{2}$$

The total winding area $A_{winding}$ can be obtained by multiplying the number of turns that are required for the desired inductance, as shown in (3).

$$A_{winding} = N.A_{w1} \tag{3}$$

Equation (4) defines the condition that must be met if the winding can fit into the available core window area, A_{window}.

$$A_{winding} < kA_{window} \tag{4}$$

DC resistance is needed to estimate the winding losses, which can be calculated using (5)

$$R = \rho \frac{l_w}{A_{winding}} \tag{5}$$

where, ρ is the resistivity of the conductor material and l_w is the length of the wire used for winding. The length of the wire comprising an n-turn winding can be expressed as

$$l_w = n(MLT) \tag{6}$$

where, MLT is the mean length per turn of the winding. The mean-length-per-turn is a function of the core geometry.

$$R = \rho \frac{n(MLT)}{A_{winding}} \tag{7}$$

Winding losses due to Joule heating are dependent on the temperature and conductor spacing in the winding. Particularly at high frequency, AC losses due to skin and proximity effect can be dominant. The AC loss effect can be determined from the ratio of AC to DC resistance, which can usually be found in the datasheet of the wire used [15]. Winding losses are estimated by using the RMS current in the winding. In this work, $J = 5\ \mathrm{A/mm^2}$ is assumed. The rationale for choosing a current density of $5\ \mathrm{A/mm^2}$ is to ensure thermal and mechanical durability for foil-type winding. The generated heat from winding losses needs to be thermally managed using natural cooling. Higher current density will result in a thinner foil winding, which will create mechanical vulnerability and thermal stress. The required winding cross-sectional area can be approximated from (2) and (3).

To calculate the winding loss, the average length of the turn has been calculated from the dimensions of the winding bobbin. The mean resistance per turn can be estimated by using the parameters like the area of copper foil and the resistivity of copper at 60 °C - 90 °C (experimental temperatures). Finally, total resistance and power losses have been calculated using the total number of turns. The inductor gap loss can be calculated using (8), assuming gap losses contributed by fringing fluxes are distributed towards the surface of the core near the airgap [16].

$$P_g = 0.0775 * l_g * E * f_s * {B_{acpp}}^2 \tag{8}$$

where l_g is the air gap length, E is the tongue width of the gap in cm, f_s is switching frequency in Hz, B_{acpp} is the peak-to-peak AC flux density in Tesla, and P_g is the gap loss in Watts.

Both the core losses and the winding losses depend on the load supplied by the converter, as both are dependent upon the current flowing through the windings. Core losses are affected by the eddy current in the magnetic core material and the alteration of the non-linear B-H curve (hysteresis effect). The effects of eddy current and hysteresis loss can be combined, and generally, the core manufacturer provides an empirical equation for calculating core loss density or sometimes provides the loss density curves. Core loss can be modelled using Generalised Steinmetz equation:

$$P_{cr} = K * f_s{}^{\alpha} * B_{acpp}{}^{\beta} \tag{9}$$

where, K is a core material coefficient, f_s is the switching frequency in kHz, B_{acpp} is the peak-to-peak AC flux density in mT and P_{cr} is the core loss in $\mathrm{mW/cm^3}$ respectively. In this paper, core losses are modelled considering METGLAS AMCC-6.3 core as depicted in (10) [16].

$$P_{cr} = 6.5 * f_{sw}{}^{1.51} * B_{acpp}{}^{1.74} \tag{10}$$

where f_s is the switching frequency in kHz, B_{acpp} is the peak-to-peak AC flux density in tesla (T) and P_{cr} is the core losses in W/kg. Generalised Steinmetz Equation (GSE) is utilised to estimate the core losses. Even though the core excitation is non-sinusoidal, the application of GSE is justified as the switching ripple is narrowband and dominated by a fundamental ripple at 80 kHz. GSE reduces the computational burden for inductor design optimisation. Moreover, the losses calculated by the GSE are validated by the temperatures estimated from the FEA analysis, as well as from the experiments at different power levels.

The estimated gap losses include the losses due to the fringe flux-induced eddy currents in the METGLAS core. However, some inaccuracies might occur in the estimation of gap losses, particularly at higher frequencies. One of the key merits of LTEC modelling is its ability to provide fast initial calculations for heat flow and temperatures. The temperature results obtained from the LTEC model using the proposed gap loss equation show fair agreement with both the FEA and experimental results, demonstrating that this method can be a reliable approach for estimating the gap losses for initial design optimisation. However, for precise gap loss estimation a more sophisticated calculations based on McLyman's equation [16] or a detailed electromagnetic FEA modelling will be required. The magnetic components are designed for a 1.5 kW interleaved DC-DC converter. AMCC-6.3 METGLAS core was used for the inductor, and E58-3F3 ferrite core was used for the IPT. Detailed designs are explained in Section IV. The losses are obtained for the designed inductor and IPT transformer using equations (1)–(10) as shown in Table 1 for the rated operating condition of the converter (12V to 48V, 1.5kW and 40 kHz).

C. FEA THERMAL MODEL SETUP

For the FEA thermal analysis of the magnetic components, the losses calculated in the previous section act as the heat source and then thermal analysis of a magnetic component can be initiated by solving the heat conduction equation described by the temperature field equation.

$$\nabla.(\lambda \nabla T) + \dot{Q} = \rho c_p \frac{\partial T}{\partial t} \tag{11}$$

TABLE 1. Estimated Losses of the Magnetic Components

Components	Input Inductor			Interphase Transformer	
Peak-to-peak AC flux density	0.0572T			0.24 T	
Losses	Winding Losses (AC+DC) [W]	Core Losses [W]	Gap Losses [W]	Winding Losses [W]	Core Losses [W]
	5.94W	5.1W	2.3W	6.25W	2.6W

TABLE 2. Anisotropic Thermal Properties Used in FEA Model

Material	Cu foil, k_{cu}	Enhanced Kapton tape, $k_{ins.}$	Air, k_{air}	Bobbin, k_{bob}
Thermal Conductivity, k (W/mK)	400	0.12	0.025	0.25
Components	Winding thermal Conductivity (W/mK)		Core thermal conductivity (W/mK)	
	$k_{winding,xy}$	$k_{winding,z}$	$k_{core,xy}$	$k_{core,z}$
DC Inductor	184.8	11.8	7.65	9
IPT	310.4	0.5	4.18	4.18

where T represents the temperature, λ is the thermal diffusivity, ρ is the material density, c_p is the specific heat capacity and $\dot{Q}$ is the volumetric heat generation.

According to the structure of magnetic components, a thermal simulation for the DC inductor and IPT transformer is conducted in COMSOL Multiphysics software. Geometric and material properties of the magnetic components are set in the model. Uniform loss distributions across the core and winding volumes are applied in the design domain.

Temperature-dependent material properties are considered in COMSOL. For simplicity, it is assumed that the sides of the magnetic component are adiabatic, and heat sources are applied at the winding and core regions. The heat transfer problem described by (11) is solved in COMSOL. To identify the hot-spot temperature, probe points are introduced in the studied magnetic components. The recorded temperatures are saved in an Excel file and later used to compare with the experimental results.

D. FEA ANALYSIS OF THERMAL MODEL

3D CAD geometric models of the designed inductor and IPT are used to create the FEA thermal model in COMSOL. Winding and core losses listed in Table 1 are used in this analysis. Since the winding region consists of many different materials such as bobbin, air, Kapton tape and copper foil. Heat flow within the winding region is anisotropic. Anisotropic thermal conductivity is applied in the model, and the properties are listed in Table 2. In the inductor, the winding region mainly covers the bobbin, air, and insulated foil winding. Typically, winding is positioned on the top of the bobbin, which is mainly plastic. Due to the very high thermal conductivity of copper, for the directions along the copper foil turns, thermal conductivity $k_{winding,xy}$ remains high. Through the copper foil

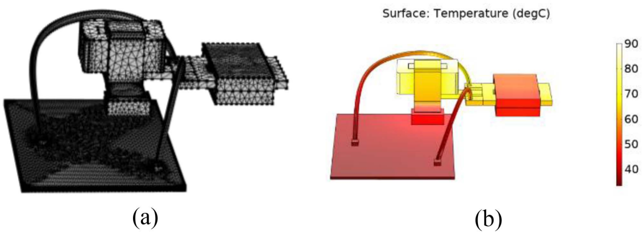

FIGURE 2. **(a) 3D mesh model of the studied magnetic components (inductor and IPT), (b) detailed temperature distribution of magnetic components in IPT-based dual interleaved bidirectional DC-DC converter.**

turns, thermal conductivity $k_{winding,z}$ remains low due to the poor thermal conductivity of air and insulating Kapton tape. The winding consists of four turns of 0.97 mm copper foil. Each copper foil turn has an insulation thickness of 0.13 mm. The winding is positioned on a plastic bobbin, which has a thickness of 2 mm. The equivalent thermal conductivity $k_{winding,xy}$ and $k_{winding,z}$ can be estimated as

$$k_{winding,xy} = \frac{k_{Cu}t_{Cu} + k_{ins}t_{ins} + k_{air}t_{air}}{t_{cu} + t_{ins} + t_{air}} \tag{12}$$

$$k_{winding,z} = \frac{t_{winding}}{(t_{cu}/k_{Cu} + t_{ins}/k_{ins})} \tag{13}$$

where t_{Cu}, t_{ins}, t_{air} are the thickness of the copper foil, insulating material and air, respectively.

k_{Cu}, k_{ins}, k_{air} are the thermal conductivities of the copper foil, insulating material and air, respectively.

Table 2 summarises the material properties used in the FEA thermal model. Since both the inductor and IPT stay outside the main circuit board (see Fig. 2) and are exposed to the ambient environment, the convective boundary condition is applied to all the surfaces exposed to ambient temperature (assumed to be 20 °C).

A detailed 3D model of winding layers (conductor + insulating kapton layer + surrounding air) would add significant complexity to the meshing of the thermal model and thus increase solution time. Therefore, the winding region is simulated as a homogenous anisotropic lumped region with corresponding thermal properties. Since the inductor and IPT are connected with DC bus bars and cables, they have been included, and a convective boundary condition is also applied to them. An equivalent heat convection coefficient is applied to all surfaces of the magnetic components. The corresponding heat transfer coefficient is 8 W/ (m^2.K) (assuming natural convection) [17]. In practice, this convection coefficient can vary between 5–15 W/m^2;·K depending on the airflow, surface orientation and surface geometry. While not explicitly studied here, this variability may lead to slight shifts in predicted temperatures. Designers are therefore recommended to consider a range of convection coefficients during FEA thermal analysis. Total node number for the FEA mesh model is about 167263. Fig. 2(a) shows the meshed model of the magnetics, while Fig. 2(b) illustrates the temperature distribution in the inductor and the IPT. Estimated maximum temperatures of the inductor core and the winding are 88.4 °C and 63.8 °C, respectively. For the IPT, the estimated maximum temperatures of the core and winding are 54.4 °C and 68.2 °C, respectively. Anisotropic heat transfer is observed for both the inductor and interphase transformer (IPT) in the temperature distribution. The temperature estimated by the FEA thermal model is compared with the experimentally measured temperature in Section IV.

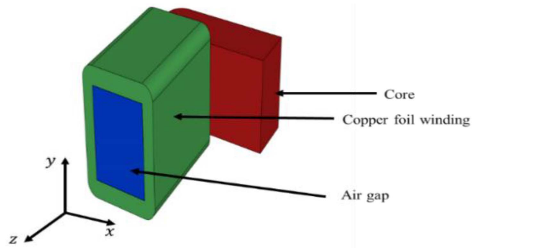

FIGURE 3. **A quarter-view of the modelled inductor.**

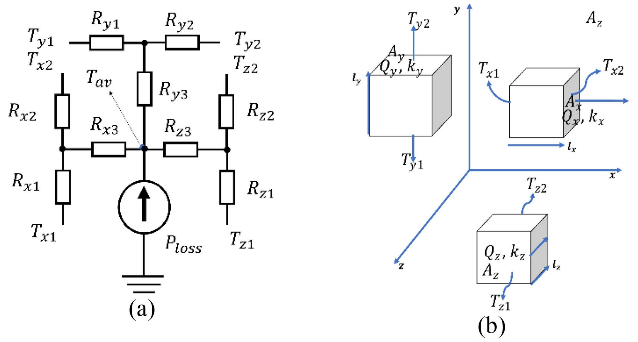

FIGURE 4. **Schematic of cuboidal element-based heat flow modelling axis (a) corresponding three-resistor T-type thermal network for three-axis (b) cuboidal elements for heat flow in three-dimensions.**

III. LUMPED THERMAL MODEL FOR INDUCTOR

An analytical thermal model is developed for one quarter of the inductor, as shown in Fig. 3. This is due to the symmetry in the dimensions of inductor parts such as core, winding, bobbin, and air gap.

The proposed thermal model has been derived using the same approach described in [5]. The lumped thermal model derived in [5] has considered the potted inductor, which was mounted on the air-cooled heatsink. The inductor designed by us is not potted and is exposed to the ambient boundary condition. Our thermal model describes the heat flow paths, such as air gap-to-bobbin, bobbin-to-winding and bobbin-to-core and core-to-winding. Our model takes into account all losses, i.e., gap losses, core losses, and winding losses.

To establish the lumped thermal model, the inductor structure is represented by a cuboidal element for each axis, where heat flow is modelled by a three-resistor T-type thermal network as shown in Fig. 4(a). The T-type network of each axis converges at a common node, which provides the average temperature, T_{av}. The heat source is labelled as P_{loss} which

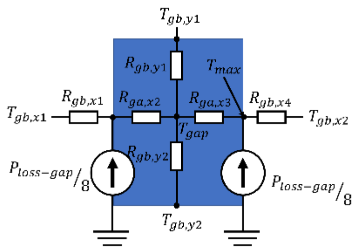

FIGURE 5. Schematic of thermal network for the heat-flow path showing air-gap-to-bobbin.

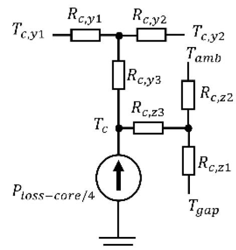

FIGURE 6. Schematic of thermal network for the heat-flow path showing the core.

is injected at the common node of the thermal network. Thermal resistances in the network are derived from solving the one-dimensional heat flow equation with internal heat source generation terms. The thermal resistances can be estimated as

$$R_{r1}, R_{r2} = \frac{l_r}{2k_rA_r}\ ,\ R_{r3} = -\frac{l_r}{6k_rA_r},\ r \in \{x, y, z\} \tag{14}$$

R_{r1} and R_{r2} are the thermal resistances for each axis, and it provide an accurate estimation of temperature when there is no consideration of internal heat source in the cuboidal element. With the help of R_{r3} the correct temperature estimation can be achieved when there is a heat source generation in a cuboidal element, and this thermal resistance is derived through superposition by solving two cases of the 1-D steady-state heat diffusion equation (a) with applying zero internal heat generation (b) considering zero surface temperatures with internal heat generation. T_{r1} and T_{r2} represent the node temperature of the cuboidal element, whilst l_r, k_r, A_r are the length, cross-sectional area and thermal conductivity of the corresponding element along the axis r, as shown in Fig. 4(b).

Air-gap-to-bobbin: Since the localised hotspot is concentrated around the airgap due to the gap loss, heat is assumed to flow from airgap to bobbin via air. The thermal network has been constructed here for the heat flow from air-gap-to-bobbin and illustrated in Fig. 5.

$T_{gb,x1}$ and $T_{gb,x2}$ represent the node temperatures of the outer and inner edges of the bobbin, whilst $T_{gb,y1}$ and $T_{gb,y2}$ represent temperatures at the top and bottom edges of the bobbin. Surface temperature at the centre of the airgap is represented as T_{gap}. In the thermal network shown in Fig. 5, $R_{ga,x2}$ and $R_{ga,x3}$ represent the thermal resistance between the edges of the core and the centre of the airgap and $R_{gb,x1}$ and $R_{gb,x4}$ represent the thermal resistance between the edges of the bobbin and the edges of the core.

$R_{gb,y1}$ and $R_{gb,y2}$ represent the y-axis thermal resistance for the gap-to-bobbin heat flow-path in the y-direction. In the z-direction, heat transfer is assumed to be negligible. The maximum heat is assumed to concentrate around the inner edge of the core face, and is approximated by the adjacent point on the bobbin, labelled as $T_{\max}$.

Core: The heat flow in the core is assumed to flow from the core to the ambient via mainly convection. A large portion of

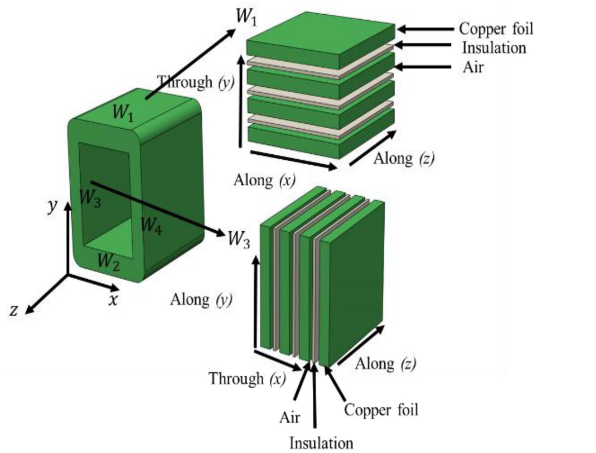

FIGURE 7. Schematic model of the DC Inductor winding showing the regions for the lumped thermal modelling, with segments of winding section W_1 and W_3 illustrating the material layers of copper foil, insulation layer (Kapton tape), and air.

the core is exposed to the ambient. It has been assumed that the core loss acts as a heat source and heat flows from the core to the airgap and then air gap to the bobbin and from the bobbin to the winding region.

The thermal network has been considered in the y- and z-axes. The core-to-ambient thermal resistance has been neglected since the region of interest is covered by airgap and bobbin, and winding. The whole thermal network is shown in Fig. 6.

Winding: Total Winding is segmented into four regions, as shown in Fig. 7, and each region is modelled as a cuboidal element. Since the winding includes different materials such as copper, air and kapton tape, anisotropic heat transfer will occur. To achieve homogeneity in each region, an effective thermal conductivity is applied, which has been calculated from the weighted average of thermal properties of the different materials. The effective thermal conductivities along the copper foil winding (x-axes and z-axes for winding section W_1 and W_2, y-axes and z-axes for winding section W_3 and W_4) are estimated as

$$k_{along} = \frac{k_{Cu}t_{Cu} + k_{ins}t_{ins} + k_{air}t_{air}}{t_{winding}} \tag{15}$$

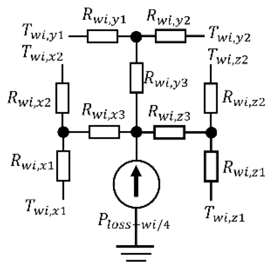

FIGURE 8. **Schematic model of the inductor winding showing the regions *W_1 - W_4*.**

The effective thermal conductivities through the winding layers, in the *y*-axis for winding sections W_1 and W_2, and *x*-axis winding sections W_3 and W_4, are calculated as

$$k_{through} = \frac{t_{winding}}{(t_{winding}/k_{Cu} + t_{ins}/k_{ins} + t_{air}/k_{air})} \tag{16}$$

where, k_{Cu} is the thermal conductivity of each foil winding, k_{ins} is the thermal conductivity of kapton tape, k_{air} is the thermal conductivity of the air, respectively. t_{Cu} is the thickness of copper foil, t_{ins} is the thickness of the insulation kapton tape, t_{air} is the gap between turns, respectively.

The thermal network for each winding section is shown in Fig. 8, where $T_{wi,x1}$, $T_{wi,x2}$,$T_{wi,y1}$ and $T_{wi,y2}$ denote the temperatures of the left, right, top and bottom faces of each winding region. $T_{wi,z1}$ denotes the temperature of the end face of each region and $T_{wi,z2}$ denotes the temperature of the symmetrical face of each region in the z-axis. Thermal resistances of each winding region in the x-axis are labelled as $R_{wi,x1}$, $R_{wi,x2}$ and $R_{wi,x3}$. Similar notations are used for the y and z axes as shown in Fig. 8.

The complete thermal model of the section of the inductor is illustrated in Fig. 9, where schematic models for core, winding, and bobbin are accumulated. The model consists of a three-dimensional thermal network of the cuboidal element considered for representing the heat-flow in core, winding, airgap- to-bobbin denoted by red, green and blue, respectively. The losses are injected into the model as heat sources, denoted by blue arrowed circles. Only a quarter of the inductor is illustrated, due to symmetry. The thermal network considered the exposed surface as the ambient temperature. The thermal network is connected to the ambient temperature as a voltage source in the lumped circuit network. The steady-state temperature can be calculated from the lumped thermal network.

Convective Boundary Conditions: Since the winding and core are exposed to ambient temperature, convective thermal resistance has been added to the corresponding thermal network. Convective thermal resistance has been estimated as

$$R_{conv} = \frac{1}{hA} \tag{17}$$

where h and A are the convective heat transfer coefficient and heat transfer area, respectively. As the calculated thermal resistances depend on the convective heat transfer coefficients of the surface, which again depend on the cooling strategies, in this work, no forced cooling is considered. However, (15) can also be used for forced air or liquid cooling by changing the convective heat transfer coefficient and calculating R_{conv} accordingly.

Using the same approach, the lumped thermal model of the interphase transformer (IPT) has been established. The LTEC model of the IPT from Simulink is shown in Fig. 10. In the IPT structure, the winding stays inside the core, and the core stays outside and exposed to the ambient (see Fig. 12). In the IPT model, a layer of air is considered since air is present between the core and the winding. Also, it has been assumed that there is air between the turns of the winding, and a large portion of the winding is exposed to the ambient (see Fig. 13). The model consists of three-dimensional thermal networks considering the heat transfer in the core region, core to winding, winding-to-ambient, and core-to-ambient regions. The predicted node temperature of the core and winding from the model is denoted by red and green circles in Fig. 10, respectively.

3D thermal resistances between core-to-winding $R_{thcwx1,}$, $R_{thcwx2,}$ $R_{thcwy,}$ and R_{thcwz} has been considered in the thermal model. Core is externally exposed to the ambient from all sides (Fig. 12). 3D thermal resistances between core-to-ambient and winding-to-ambient are denoted by R_{thcay}, $R_{thcaz,}R_{thwaz}$, R_{thway}. Core loss and winding losses have been applied as a heat source in the thermal model. All the surfaces are exposed to the ambient, and the ambient temperature is set to 20 °C. Results from the LTEC models are discussed in Section IV.

IV. EXPERIMENTAL VALIDATIONS

An experimental study is conducted to further demonstrate the effectiveness of the proposed thermal modelling method. A 1.5 kW dual-interleaved bidirectional DC-DC converter is designed and built for interfacing the 12V and 48V systems of an electric vehicle. The switching frequency of the converter was 40 kHz. The converter schematic is presented in Fig. 11. Here, L_{in} is the filter inductor, and IPT is an interphase transformer coupling the two phases of the converter. The inductor is designed using amorphous alloy cores (METGLAS) and copper foil-based winding. The IPT is designed based on ferrite cores and flat copper foil windings. The switching devices of the converter (T1-T4) are Si CoolMOS MOSFETs from Infineon in the DirectFET L8 package (IRF7759L2TRPBF). The input and output capacitors are based on MLCC capacitors. Ten C1210C475M1R2CTU (4.7μF dual MLCC stack) capacitors connected in parallel were used as $C_{out,}$ and four of them connected in parallel were used as C_{in}. The circuit is constructed on top of a T-Clad board.

To design the inductor, two METGLAS AMCC-6.3 C cores were connected with pieces of plastic shim between them to create the required air gap (0.61 mm). A copper foil of 23mm width and 0.97mm thickness was used to make the four turns for the inductor. Kapton was used to create inter-winding insulation. After the final assembly, the inductor was tested using an LCR meter. The inductance and AC resistance were

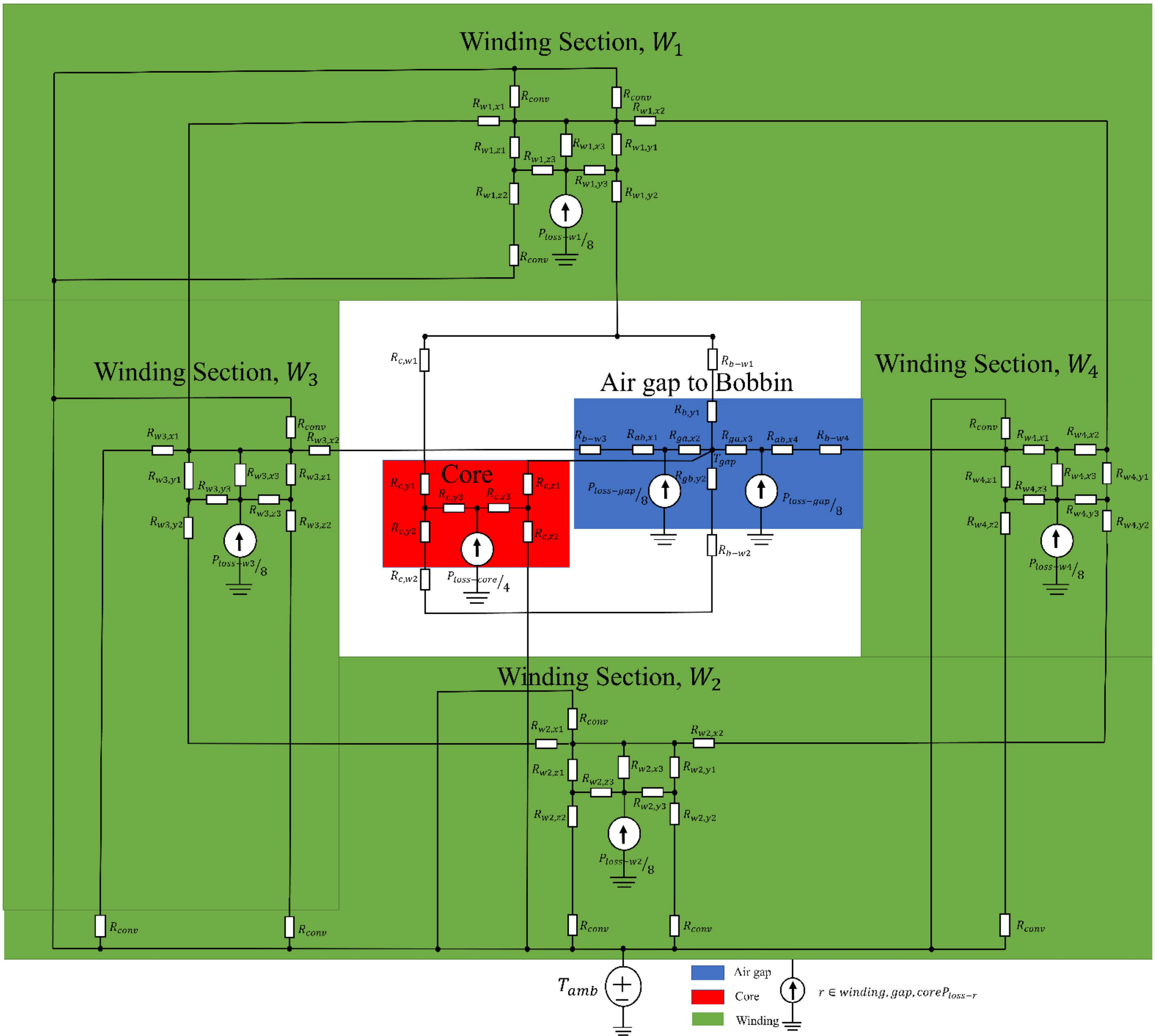

FIGURE 9. Lumped thermal equivalent circuit model of the inductor.

found to be 6.71 μH and 0.127 Ω for 80 kHz operation, respectively. Due to the interleaving, the inductor current ripple has a frequency twice that of the switching frequency.

One E58-3F3 ferrite core was attached to a PLT58-3F3 ferrite core with a 0.1mm plastic shim between them to create the IPT. The four flat turns were made from a copper sheet of 0.45mm thickness. At first, four rectangular copper plates were stamped out from a copper sheet (see Fig. 12(a)). Then all of them were cut at a specific distance from the edge to form the individual turns. Then all the turns were soldered in a sequence so that a complete winding was shaped. Finally, three tags were connected at appropriate positions to form the three terminals of IPT. After the fabrication of the winding, Kapton film was used to insulate the turns. The schematics and dimensions of four individual turns are also shown in Fig. 12. After assembling the winding with the core, the IPT was tested using an LCR meter. The differential inductance was found to be 24.5 μH for 40 kHz operation. The leakage inductances for the two windings, L11 and L22, were found to be 0.376 μH and 0.345 μH, respectively. The low leakage inductance compared to the total differential inductance justified high coupling between the IPT windings, which was an essential criterion for the design to remove the DC flux from the core. Finally, IPT open circuit tests were done, and the inductance values for L11 and L22 were found to be 6.3 μH and 6.25 μH, respectively. The ambient temperature in the lab was 20 °C.

Fig. 13 shows the completed 1.5 kW converter. Cables rated at 150A were used for connecting the IPT to the T-Clad board. Inductor terminals are directly connected to the T-Clad board and the IPT mid-point tab. A variable resistor bank (resistive load changing from 1.5 Ω to 18.5 Ω) was used to test the converter. The converter was tested for a power range of 124.5W to 1500W, considering the 12V to 48V operation. An external gate driving circuit was used to drive the MOSFETs.

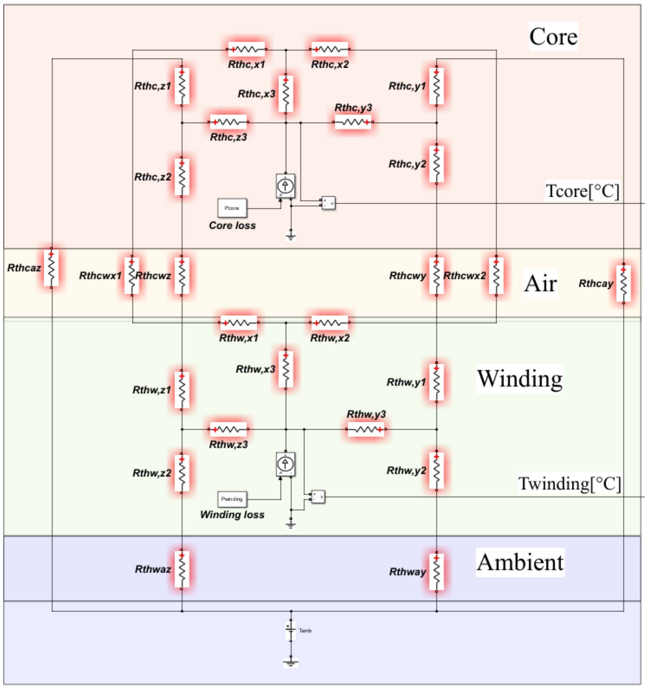

FIGURE 10. Lumped-thermal equivalent circuit (LTEC) of IPT (half structure considered due to symmetry).

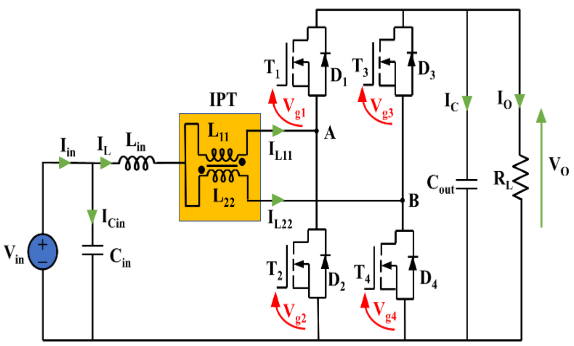

FIGURE 11. A 12V to 48V dual-interleaved DC-DC converter.

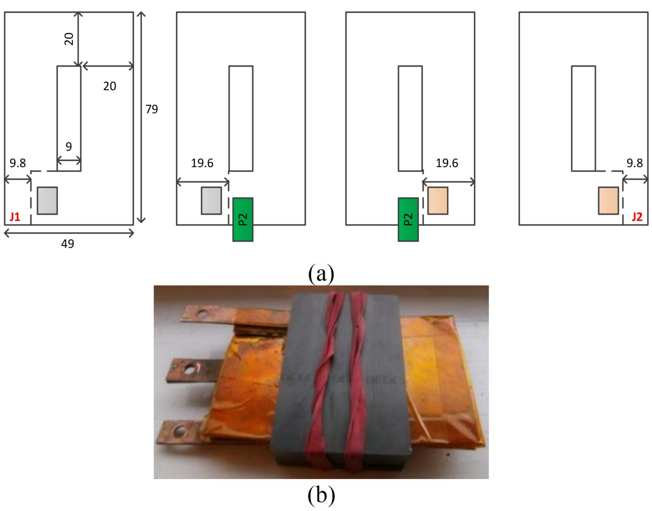

FIGURE 12. (a) Four individual IPT turns, their dimensions and inter-connecting points (all dimensions in mm) and (b) the constructed IPT.

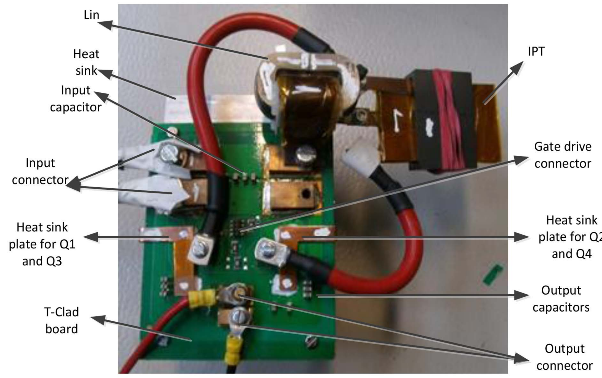

FIGURE 13. Completed 12V to 48V DC-DC converter.

Two current probes were connected in two IPT windings to measure the IPT winding currents. By adding them, the inductor current can be observed. Necessary voltage probes and multi-meters were also connected during experiments to measure the critical waveforms. An infrared imaging camera was used to monitor the components' temperature.

Since the METGLAS and ferrite cores of the studied magnetic components seem to appear as naturally dark, matte surfaces, their emissivity was set to 0.9 for IR thermography. Although the use of ceramic spray/black paint/high emissivity tape can significantly improve the accuracy of temperature measurement by IR thermography, as a high-bandwidth infrared thermal camera (FLUKE TiS 10) was used to observe the temperature distribution and the temperature was validated for various power conditions, no additional paints on the magnetic components were added. The purpose of the IR thermal camera-based measurement was to capture the heat distribution spread across the core, particularly near the air gap and further to compare with the FEA provided temperature distribution.

Experimental waveforms for the 1.5 kW Boost operation are shown in Fig. 14. The losses in the magnetic components are calculated based on these experimental waveforms and the equations shown in Section II-B. Inductor and IPT losses are similar to the predicted losses shown in Table 1. Inductor and IPT temperatures for 1.5 kW boost-mode operation are shown in Fig. 15. Maximum core temperature for the inductor was 89.1 °C, and for the IPT was 56.2 °C. The maximum winding temperature for the inductor was 64.3 °C, and for the IPT was 67.3 °C. Maximum winding temperature estimated for the inductor from the lumped thermal model shown in Fig. 9 was 69.1 °C, while core temperature was found to be 89.4 °C. The maximum winding temperature estimated for the IPT from the lumped thermal model shown in Fig. 10 was 69.7 °C, while the core temperature was found to be 59.4 °C. Therefore, results obtained from the lumped thermal model match experimental results with a maximum error of 4.8 °C. The maximum error between the experiment and FEA simulation for the inductor and IPT was 2 °C and 4 °C, respectively. The comparison is shown in Table 3. The results suggest that LTEC models accurately predicted the hotspot temperature

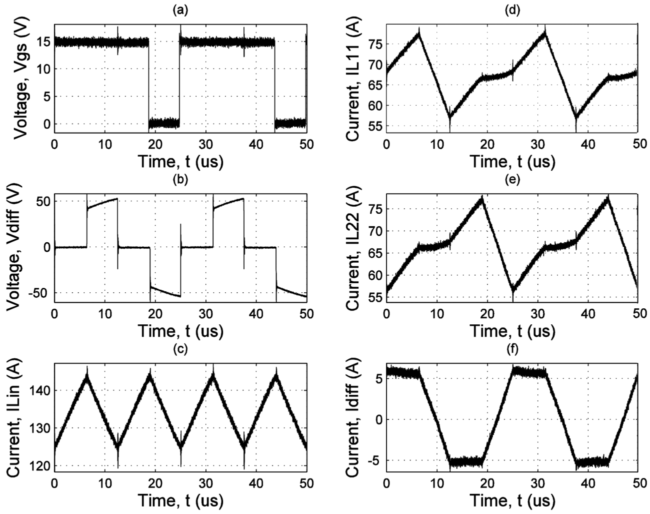

FIGURE 14. Steady state waveforms from the converter at rated operating condition: D = 75.64% , V_{in} =11.8 V, V_o =45.55 V, I_{in} = 134 A, and I_o = 32.5 A. (a) Gate to source voltage, V_{gs}, (b) Differential voltage across IPT, V_{diff} , (c) Input inductor current, I_{Lin} , (d) IPT winding-L11 current, I_{L11}, (e) IPT winding-L22 current, I_{L22}, and (f) IPT differential current, I_{diff}.

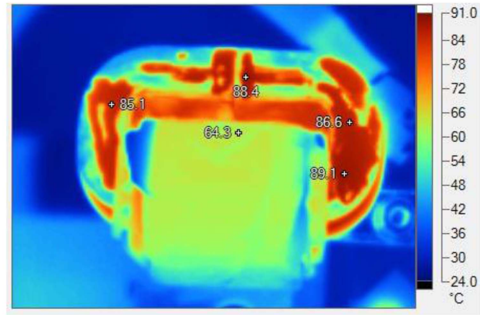

(a)

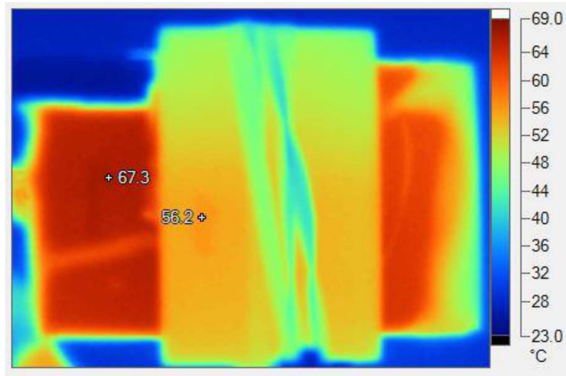

(b)

FIGURE 15. Temperature distribution at 1.5 kW load power of the converter for (a) inductor, Lin, (b) interphase transformer, IPT.

TABLE 3. Comparison of the Predicted Temperature of the Magnetic Components At the Rated Operating Conditions (1500 W)

Components	Inductor temperature		Interphase Transformer	
Modelling Method	Winding Temperature °C	Core temperature °C	Winding Temperature °C	Core Temperature °C
Experimental	64.3	89.1	67.2	56.2
FEA	63.8	89.5	68.2	52.1
LTEC	**69.1**	**89.4**	**69.7**	**59.4**

TABLE 4. Performance Comparison of the Proposed LTEC, FEA and Experimental Thermal Modelling Methods

Thermal Model Type	LTEC	FEA	Experimental
Model construction time	Low	High	Extremely High
Computational effort	Low [<1s]	High[30minutes ~2hours]	Highest [>1-2 hours]
Model complexity	Low	High	High
Accuracy	Moderate	High	Highest
Software requirements	MATLAB/Simulink	ANSYS/COMSOL	IR Thermal Camera/Thermocouples/data acquisition system
Scalability	Easy to parameterise	Time consuming	Physical retesting needed
Integration with circuit simulation	Easy	Difficult	Not Possible
Validation requirement	Needs experimental data	Needs experimental data	Acts as a benchmark

for both the inductor and the IPT. The reason for the small error is the simplified anisotropic assumption for foil winding. Although material properties like thermal conductivity change with temperature, for the LTEC modelling, a constant average value is chosen to facilitate a fast initial estimation of the hot-spot temperatures for the magnetic components. As the temperature-dependent changes to the thermal conductivity are small in the tested temperature range (40–85°), fairly accurate results are found from the LTEC models. A comparative performance analysis of LTEC, FEA and Experimental methods is shown in Table IV. The benefits of LTEC modelling are low computational effort, low complexity and high scalability compared to FEA.

The maximum error in the LTEC model occurred for the inductor winding. It has been assumed that the inductor winding is not connected to the heatsink. However, it is evident from Fig. 13 that one terminal is connected with the copper terminal block, which is bolted to the IMS board. Another limitation is that the LTEC model cannot provide accurate information about the specific location of the localised hotspot. For example, the proposed inductor LTEC model considers the gap as a single node at the centre of the gap. The inductor hotspot is observed experimentally at the gap edges, on the core surfaces, while the FEA thermal model identified a localised hotspot slightly inside the core. The reason is that the gap losses contributed by fringing fluxes are distributed towards the surface, but in the simulation, homogeneous volumetric heat loss is applied to represent them. Temperature predicted near the gap by the thermal models, either LTEC or FEA, due to anisotropic assumptions, may not be sufficiently accurate for reliable converter design in terms of worst-case thermal

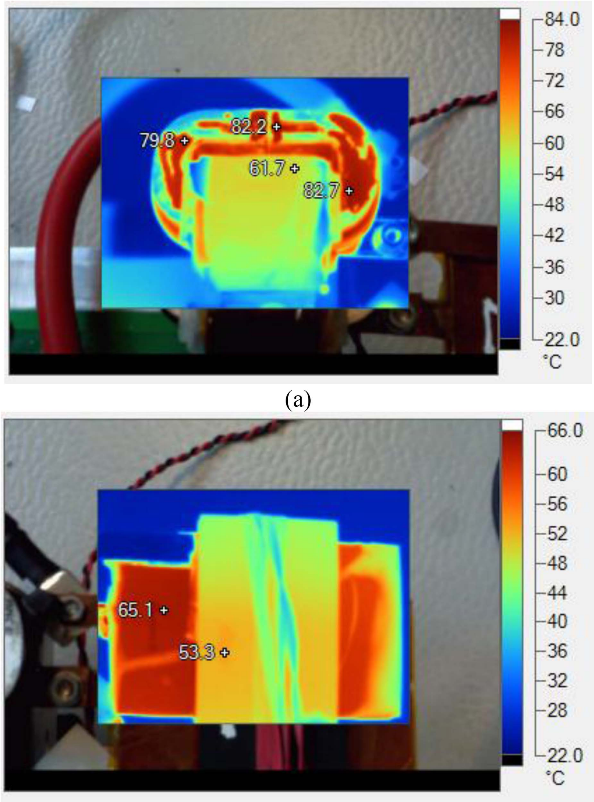

FIGURE 16. **Temperature distribution at 1.3 kW load power of the converter for (a) inductor, L_{in}, (b) interphase transformer, IPT.**

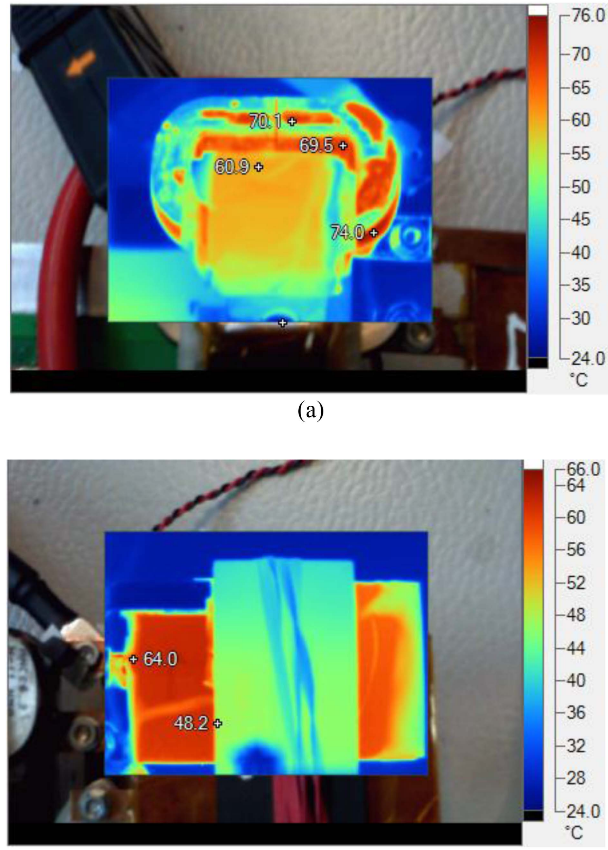

FIGURE 17. **Temperature distribution at 1.2 kW load power of the converter for (a) inductor, Lin, (b) interphase transformer, IPT.**

tolerance. Therefore, an additional thermal safety margin of at least 10 °C is recommended for practical converter designers. If the gap temperature still exceeds core demagnetisation temperature limits, use of high-thermal-conductivity heat spreaders near the gap is also recommended as part of thermal management.

Although the validation of the LTEC models is based on the 1.5 kW converter, as two different core materials and two different geometries are considered in this study, and the temperature predictions are fairly accurate for both the inductor and the IPT, this method can be extended for magnetics with different cores and converter topologies. For different power scales and topologies, differences will be the change in the loss equations; thus, LTEC models are reproducible. Thermal results at different power levels of the converter are shown in Figs. 16–18 for 1.3 kW, 1.2 kW and 0.9 kW conditions, respectively. Inductor and IPT temperatures for 1.3 kW boost-mode operation are shown in Fig. 16. Maximum core temperature for the inductor was 82.7 °C, and for the IPT was 53.3 °C. Maximum winding temperature for the inductor was 61.7 °C, and for the IPT was 65.1 °C. Maximum winding temperature estimated for the inductor from the lumped thermal model shown in Fig. 9 was 66.4 °C, while core temperature was found to be 82.3 °C. Maximum winding temperature estimated for the inductor from the lumped thermal model shown in Fig. 10 was 67.9 °C, while core temperature was found to be 58.4 °C. Therefore, results obtained from the lumped thermal model match with experimental results with a maximum error of 5 °C for the inductor and 8 °C for the IPT. Results from different power levels are summarised in Table 5. These results confirmed that the proposed LTEC modelling works at different power levels for both the inductor and the IPT. The LTEC modelling is scalable to different operating frequencies, given that the core and winding losses are calculated accurately at the operating frequencies.

TABLE 5. **Temperatures at Different Operating Conditions**

Load Power (kW)	Type	Inductor (°C)		Interphase Transformer (°C)	
		Core	Winding	Core	Winding
1.5	Experimental	89.1	64.3	56.2	67.3
	FEA	89.5	63.8	52.1	68.2
	LTEC	**89.4**	**69.1**	**59.4**	**69.7**
1.3	Experimental	82.7	61.7	53.3	65.1
	FEA	84.7	67	52.1	69.6
	LTEC	**82.3**	**66.4**	**58.4**	**67.9**
1.2	Experimental	74	60.9	48.2	64
	FEA	68.8	55.1	52.1	55.8
	LTEC	**66.1**	**54.4**	**53.3**	**57.8**
0.9	Experimental	49.5	39.3	41.2	43.9
	FEA	52.1	40.7	48.5	40.8
	LTEC	**44.3**	**38.1**	**46.08**	**43.8**

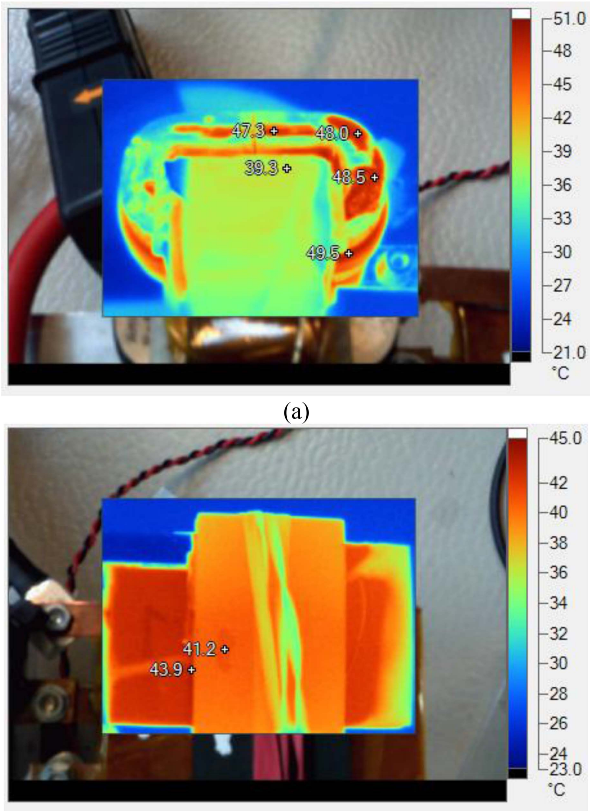

(a)

(b)

FIGURE 18. Temperature distribution at 0.9 kW load power of the converter for (a) inductor, Lin, (b) interphase transformer, IPT.

V. CONCLUSION

In this work, a lumped thermal equivalent circuit (LTEC) model for analysing magnetic components at the design stage has been presented. LTEC models can provide precise node temperatures in the region of interest of a magnetic component. The key challenge for accurate modelling of the temperature for magnetics is identifying accurate thermal resistances for the heat-path in various regions, including core-to-core, core-to-airgap, winding-to-airgap, core-to-winding, and winding-to-air. The proposed LTEC-guided magnetic component design has been validated by comparing simulation results with FEA thermal simulations and experimental results from a 1.5 kW DC-DC interleaved boost converter.

For the filter inductor, the LTEC results are comparable to the experimental results, with an error of 7.4% at 1.5 kW power. In contrast, for the IPT, the error reaches up to 5.7% when compared with the experimental results at 1.5 kW power. Although the FEA model provides a better temperature distribution and better estimation of localised hotspots, it is not suitable for design optimisation since it needs high computational power, which is burdensome for design optimisation tasks where rapid evaluation of numerous design variants must be performed. Therefore, LTEC models for magnetic components can be used for a real converter design due to their fast and accurate temperature prediction and extendibility to explore the design space for optimisation. Validation of the LTEC modelling for different magnetic components (inductors and IPT) with different core geometries and materials establishes the universal application of the method for design optimisation of magnetic components. The methodology can also be extended for assessing the reliability of magnetic components for high-current, high-frequency converter applications, which will enable virtual designs for power electronics converters.

REFERENCES

[1] T. M. Andersen et al., “Modeling and Pareto optimization of on-chip switched-capacitor converters,” *IEEE Trans. Power Electron.*, vol. 32, no. 1, pp. 363–377, Jan. 2017.
[2] B. J. Masserant, E. W. Beans, and T. A. Stuart, “A study of volume versus frequency for soft-switching IGBT converters,” *IEEE Trans. Aerosp. Electron. Syst.*, vol. 31, no. 1, pp. 280–287, Jan. 1995.
[3] R. Wrobel, N. McNeill, and P. H. Mellor, “Performance analysis and thermal modeling of a high-energy-density prebiased inductor,” *IEEE Trans. Ind. Electron.*, vol. 57, no. 1, pp. 201–208, Jan. 2010.
[4] G. M. Shane and S. D. Sudhoff, “Design paradigm for permanent-magnet-inductor-based power converters,” *IEEE Trans. Energy Convers.*, vol. 28, no. 4, pp. 880–893, Dec. 2013.
[5] A. Behniafar, M. Mokhtari, and M. Moallem, “A machine-learning-based strategy for online prediction of dry-type three-phase transformer temperatures,” *Appl. Sci.*, vol. 15, no. 3, pp. 110490, 2025.
[6] Y. Li, J. Zhou, and H. Liu, “An LSTM neural network prediction model of ultra-short-term transformer winding hotspot temperature,” *AIP Adv.*, vol. 15, no. 2, 2025, Art. no. 025202.
[7] U. Salaberria-Flaño, A. Nappa, A. Artetxe, G. Artetxe, and I. Inza, “SCGAN-enhanced surrogate modeling for FEM analysis of induction motors: A practical use case,” *Results Eng.*, vol. 27, 2025, Art. no. 106061, doi: 10.1016/j.rineng.2025.106061.
[8] J. Scoltock, Y. Wang, G. Calderon-Lopez, and A. J. Forsyth, “Rapid thermal analysis of nanocrystalline inductors for converter optimization,” *IEEE J. Emerg. Sel. Topics Power Electron.*, vol. 8, no. 3, pp. 2276–2284, Sep. 2020.
[9] N. Simpson, R. Wrobel, and P. H. Mellor, “An accurate mesh-based equivalent circuit approach to thermal modeling,” *IEEE Trans. Magn.*, vol. 50, no. 2, Feb. 2014, Art. no. 7006504.
[10] R. Wrobel and P. H. Mellor, “Thermal design of high-energy-density wound components,” *IEEE Trans. Ind. Electron.*, vol. 58, no. 9, pp. 4096–4104, Sep. 2011.
[11] R. Wrobel and P. H. Mellor, “A general cuboidal element for three-dimensional thermal modelling,” *IEEE Trans. Magn.*, vol. 46, no. 8, pp. 3197–3200, Aug. 2010.
[12] R. Shafaei, M. C. G. Perez, and M. Ordonez, “Planar transformers in LLC resonant converters: High-frequency fringing losses modeling,” *IEEE Trans. Power Electron.*, vol. 35, no. 9, pp. 9632–9649, Sep. 2020.
[13] J. Muhlethaler, J. Biela, J. W. Kolar, and A. Ecklebe, “Core losses under the DC bias condition based on Steinmetz parameters,” *IEEE Trans. Power Electron.*, vol. 27, no. 2, pp. 953–963, Feb. 2012.
[14] Y. Wang, G. Calderon-Lopez, and A. J. Forsyth, “Thermal management of compact nanocrystalline inductors for power-dense converters,” in *Proc. IEEE Appl. Power Electron. Conf. Expo.*, Mar. 2018, pp. 2696–2703.
[15] N. Simpson, R. Wrobel, and P. H. Mellor, “Multi-physics design of high-energy-density wound components,” in *Proc. IEEE Energy Convers. Congr. Expo.*, Sep. 2015, pp. 3857–3864.
[16] C. W. T. McLyman, *Transformer and Inductor Design Handbook*. Boca Raton, FL, USA: CRC Press, 2004.
[17] T. L. Bergman, *Fundamentals of Heat and Mass Transfer*. Hoboken, NJ, USA: Wiley, 2011.

MOHAMMAD SHAHJALAL received the B.Sc. degree in electrical and electronics engineering from the Chittagong University of Engineering and Technology, Chittagong, Bangladesh, in 2009, the M.Sc. degree in digital image and signal processing from the University of Manchester, Manchester, U.K., in 2013, and the Ph.D. degree in computing and mathematical sciences from the University of Greenwich, Greenwich, U.K., in 2018. From 2010 to 2012, he was a Lecturer with the Department of Electrical and Electronics Engineering, International Islamic University of Chittagong, Chittagong. From 2018 to 2021, he led the project "Thermal (entropic heat) characterization of Li-ion pouch cells in BEV with WMG". He is currently a Visiting Research Fellow with the School of Computing and Mathematical Sciences, University of Greenwich. His current research interests include electrothermal modelling of power semiconductor devices, packaging, and reliability of power electronic converter systems and components like Si/SiC/GaN based power modules and electro-thermal modelling of energy storage driven converter system in wide application.

UVAIS MUSTAFA (Member, IEEE) received the B.Tech. in electrical engineering and the M.Tech. degree in instrumentation and control with a gold medal from Aligarh Muslim University, India, in 2016 and 2019, respectively. He is currently working toward the Ph.D. degree with the Power Electronics, Machines and Control Research Institute, University of Nottingham, Nottingham, U.K. His research interests include the reliability of power electronic converters, health monitoring, converter topologies, and applications of power electronics in renewable energy systems. His work aims to improve the durability and performance of modern power conversion systems used in sustainable energy infrastructures.

STOYAN STOYANOV (Senior Member, IEEE) received the B.Sc. degree in mathematics and the M.Sc. degree in applied mathematics from Sofia University, Sofia, Bulgaria, in 1994 and 1996, respectively, and the Ph.D. degree in computational engineering from the University of Greenwich, London, U.K., in 2004. In 2004, he joined the Computational Mechanics and Reliability Group, School of Computing and Mathematical Sciences, University of Greenwich, where he advanced his professional career. In 2010, he was promoted from the position of a Senior Research Fellow to a Reader of computational engineering and optimization. He is currently a Professor of computational engineering and optimisation, University of Greenwich. He has authored or coauthored more than 120 peer-reviewed articles. His research interests include the development and application of modeling and simulation tools for numerical analysis of the performance and reliability of electronics products and microsystems, physics-of-failure modeling, computational intelligence for data-driven and prognostics modeling, additive manufacturing, and design optimization. He is a member of the IEEE Electronics Packaging Society, the Steering Committee of the IEEE International Spring Seminar on Electronics Technology, and the technical committee of several IEEE conferences such as ISSE, EMPC, and ESTC.

MD. RISHAD AHMED (Member, IEEE) received the B.Sc. degree from the Bangladesh University of Engineering and Technology, Dhaka, Bangladesh, in 2011, and the M.Sc. (Hons.) and Ph.D. degrees from the University of Manchester, Manchester, U.K., in 2013 and 2017, respectively. Prior to joining the University of Nottingham, Nottingham, U.K., as an Assistant Professor, in 2020, he was a Design Engineer with Dynex Semiconductor, Lincoln, U.K., for 2.5 years. He is currently an Associate Professor of power electronics with PEMC Research Institute, University of Nottingham. His research interests include high-frequency converters, wide bandgap semiconductor devices, passive components, and converter packaging. He has authored more than 60 papers and two patents on power converter technologies.